

The spectroscopic orbits and the geometrical configuration of the symbiotic binary AR Pavonis^{*}

C. Quiroga^{1,2}, J. Mikolajewska³, E. Brandi^{2,4}, O. Ferrer^{1,2} and L. García²

¹ Consejo Nacional de Investigaciones Científicas y Técnicas de la República Argentina (CONICET)

² Facultad de Ciencias Astronómicas y Geofísicas - Universidad Nacional de La Plata - La Plata - Argentina

³ Copernicus Astronomical Center- Warsaw - Poland

⁴ Comisión de Investigaciones Científicas de la Provincia de Buenos de Aires (CIC) - Argentina

Received / Accepted

Abstract. We analyze optical and near infrared spectra of intermediate and high resolution of the eclipsing symbiotic system AR Pavonis. We have obtained the radial velocity curves for the red and the hot component from the M-giant absorption lines and from the wings of H α , H β and He II λ 4686 emission profiles, respectively. From the orbital elements we have derived the masses, $M_g = 2.5M_\odot$ and $M_h = 1.0M_\odot$, for the red giant and the hot component, respectively. We also present and discuss radial velocity patterns in the blue cF absorption spectrum as well as various emission lines. In particular, we confirm that the blue absorption lines are associated with the hot component. The radial velocity curve of the blue absorption system, however, does not track the hot companion's orbital motion in a straightforward way, and its departures from an expected circular orbit are particularly strong when the hot component is active. We suggest that the cF-type absorption system is formed in material streaming from the giant presumably in a region where the stream encounters an accretion disk or an extended envelope around the hot component. The broad emission wings originate from the inner accretion disk or the envelope around the hot star. We also suggest that the central absorption in H profiles is formed in a neutral portion of the cool giant's wind which is strongly concentrated towards the orbital plane. The nebula in AR Pav seems to be bounded by significant amount of neutral material in the orbital plane. The forbidden emission lines are probably formed in low density ionized regions extended in polar directions and/or the wind-wind interaction zone.

Key words. stars: binaries: eclipsing – binaries: symbiotic – stars: fundamental parameters – stars: individual: AR Pav

1. Introduction

The symbiotic star AR Pavonis was discovered by Mayall (1937) as an eclipsing binary with a period of 605 days. The eclipsed object is highly variable in both brightness and size (Andrews 1974). Thackeray & Hutchings (1974, hereafter TH74) based on extensive analysis of spectroscopic data spanning several orbital cycles proposed a binary model for AR Pav with the M3 III secondary filling its Roche lobe. They found that the eclipsed primary shows an emission O-type spectrum and density and ex-

citation in the eclipsed region increasing towards the central primary light source. TH74 derived masses of order $2.5M_\odot$ and $1.2M_\odot$, for the primary and secondary, respectively. Their estimate was based on analysis of the eclipse shape, and the primary mass function derived from radial velocities of almost exclusively He I emission lines. In particular, they did not measure radial velocities for the cool giant. TH74 also found periodic changes in radial velocities of forbidden lines and cF-type absorption lines, which they attributed to a stream and a region where the stream falls on a ring/disk surrounding the primary. Kenyon & Webbink (1984) revised this model involving an accretion disk around a main sequence star as the primary light source.

Bruch et al. (1994) observed dramatic variations in the visual light curve between eclipses which are not easily explained by the TH74 model. They suggested variations in the mass transfer rate from the red giant to the hot component as the most satisfying explanation. Skopal et al.

Send offprint requests to: C. Quiroga, e-mail: claudioq@muchi.fcaglp.unlp.edu.ar

* Based on observations taken at Complejo Astronómico El Leoncito (CASLEO), operated under an agreement between the Consejo Nacional de Investigaciones Científicas y Técnicas de la República Argentina, the Secretaría de Ciencia y Tecnología de la Nación and the National Universities of La Plata, Córdoba and San Juan

Table 1. Log of the spectroscopic observations of AR Pav

Date	JD(2400000+)	Phase	Detector	Range (Å)
4/08/90	48117.7	0.966	Z M	5850-7200
06/11/90	48201.5	0.105	Z M	5850 7100
08/11/90	48204.5	0.110	Z M	4380-5050
06/04/91	48352.8	0.355	Z M	5800-7100
07/04/91	48353.8	0.356	Z M	4400-5050
17/08/92	48852.7	0.182	T CCD	8300-9000
19/06/95	49887.7	0.894	R CD ¹	4820-7800
19/06/95	49887.8	0.894	R CD ¹	4820-7800
12/08/95	49941.7	0.983	R CD ¹	4230-7300
06/03/98	50879.9	0.535	R CD ¹	4320-7350
07/03/98	50880.9	0.537	R CD ¹	4320-7350
30/05/98	50963.9	0.674	BC	3900-5020
07/09/98	51064.6	0.841	R CD ¹	5750-8750
12/09/98	51069.6	0.849	R CD ²	4075-7100
01/03/99	51238.9	0.129	R CD ¹	4625-7550
26/05/99	51324.8	0.271	R CD ¹	4550-7550
01/09/99	51422.6	0.433	R CD ¹	5700-8700
02/09/99	51423.7	0.435	R CD ¹	4250-7300
03/09/99	51424.5	0.436	R CD ¹	4250-7300
25/03/00	51628.9	0.774	R CD ¹	4450-7550
27/03/00	51630.9	0.778	R CD ¹	4450-7550
29/07/00	51754.7	0.982	R CD ¹	4000-7100
31/07/00	51756.7	0.986	R CD ¹	5500-8700

Z M: Reticon Z-Machine

T CCD: Thompson CCD (384x576 pixels)

R CD: REOSC echelle spectrograph in cross-dispersion

BC: Boller & Chivens spectrograph

1 images taken with bin factor=2

2 image taken with bin factor=4

(2000a) noted that the AR Pav light curve has a characteristic shape similar to those of dwarf novae in quiescent phase; whereas during the active phases the profile of the light curve changes considerably.

The first orbital solution for the cool giant has been recently obtained by Schild et al. (2001, hereafter S01). They also measured the rotation velocity of the giant, and, assuming co-rotation, its radius. Based on this radius combined with the known spectral type of the giant and the corresponding effective temperature S01 estimated the giant's luminosity and distance to AR Pav, as well as from the position in the HR diagram the giant's mass. Their binary mass function then resulted in masses of $2 M_{\odot}$ and $0.75 M_{\odot}$ for the cool giant and its hot companion, respectively.

In this paper we present new radial velocity data for the cool giant and the emission lines collected between 1990 and 2000. From this we derive new spectroscopic orbits for both components, and discuss the velocity patterns in various emission lines.

2. Observations

Spectroscopic observations were performed with the 2.15 m telescope of Complejo Astronómico el Leoncito,

CASLEO (San Juan, Argentina). During 1990 and 1991 medium-low resolution spectra were taken with a Boller & Chivens Cassegrain spectrograph using a photon-counting Reticon, called Z-Machine ($\lambda/\Delta\lambda=4100$ and 2700 in the filters blue and red respectively), and a Thompson CCD of 384×576 pixels ($\lambda/\Delta\lambda=2600$) in 1992. Since 1995, high resolution spectra were obtained with a REOSC echelle spectrograph using a Tek CCD 1024×1024 pixels ($\lambda/\Delta\lambda=15000$), except in May 1998 when a spectrograph Boller & Chivens was used. Table 1 shows a log of the observations.

Barbá et al. (1992) describe details of the Z-Machine, acquiring and reducing data procedures. The CCD data were reduced with IRAF¹ packages, CCDRED and ECHELLE and all the spectra were measured using the SPLOT task within IRAF.

To obtain the flux calibration, standard stars from Stone & Baldwin (1983) and Baldwin & Stone (1984) were observed each night. A comparison of the spectra of the standards suggests that the flux calibration errors are about 15 per cent for the Z-Machine and 20 per cent in the central part of each order for the REOSC echelle images.

In the determination of the hot component orbit, we have included the $H\alpha$ and He II $\lambda 4686$ profiles measurements from a spectrum taken by Van Winckel (1993), in July 1988 and corresponding to phase $\phi = 0.72$.

3. Analysis and discussion

3.1. Emission line profiles

The left panel of Fig. 1 shows the $H\alpha$ emission line profiles of AR Pav ordered with their orbital phase, although they are collected from more than one cycle. $H\alpha$ is strongest in phase 0.54, when the hot component is in front. The profiles are double-peaked with broad, $FW \gtrsim 1600 \text{ km s}^{-1}$, wings. The red peak is stronger than the blue one in all phases. This can not be explained by motions in an optically thin medium. In such situation the profile of the second quadrature would be reversed relative to the first quadrature. The profiles are apparently affected by self-absorption. The largest blue to red peak intensity ratio is observed around phases 0.13 and 0.27, respectively, whereas the smallest value of this ratio corresponds to phase 0.77. The double-peaked profiles have an average separation of $148 \pm 3 \text{ km s}^{-1}$. The average radial velocity of the central absorption is $-96 \pm 1 \text{ km s}^{-1}$. In eclipse, $H\alpha$ profiles are considerably narrower than out of eclipse (**Fig. 2**). This suggest that the broad $H\alpha$ wings are formed near to the hot component.

The shape of $H\beta$ profile is similar to that of $H\alpha$, but the blue to red peak intensity ratio is smaller than the same ratio for $H\alpha$, except for phases 0.98 to 0.13, when

¹ IRAF is distributed by the National Optical Astronomy Observatories, which is operated by the association of Universities for Research in Astronomy, INC., under contract to the National Science Foundation

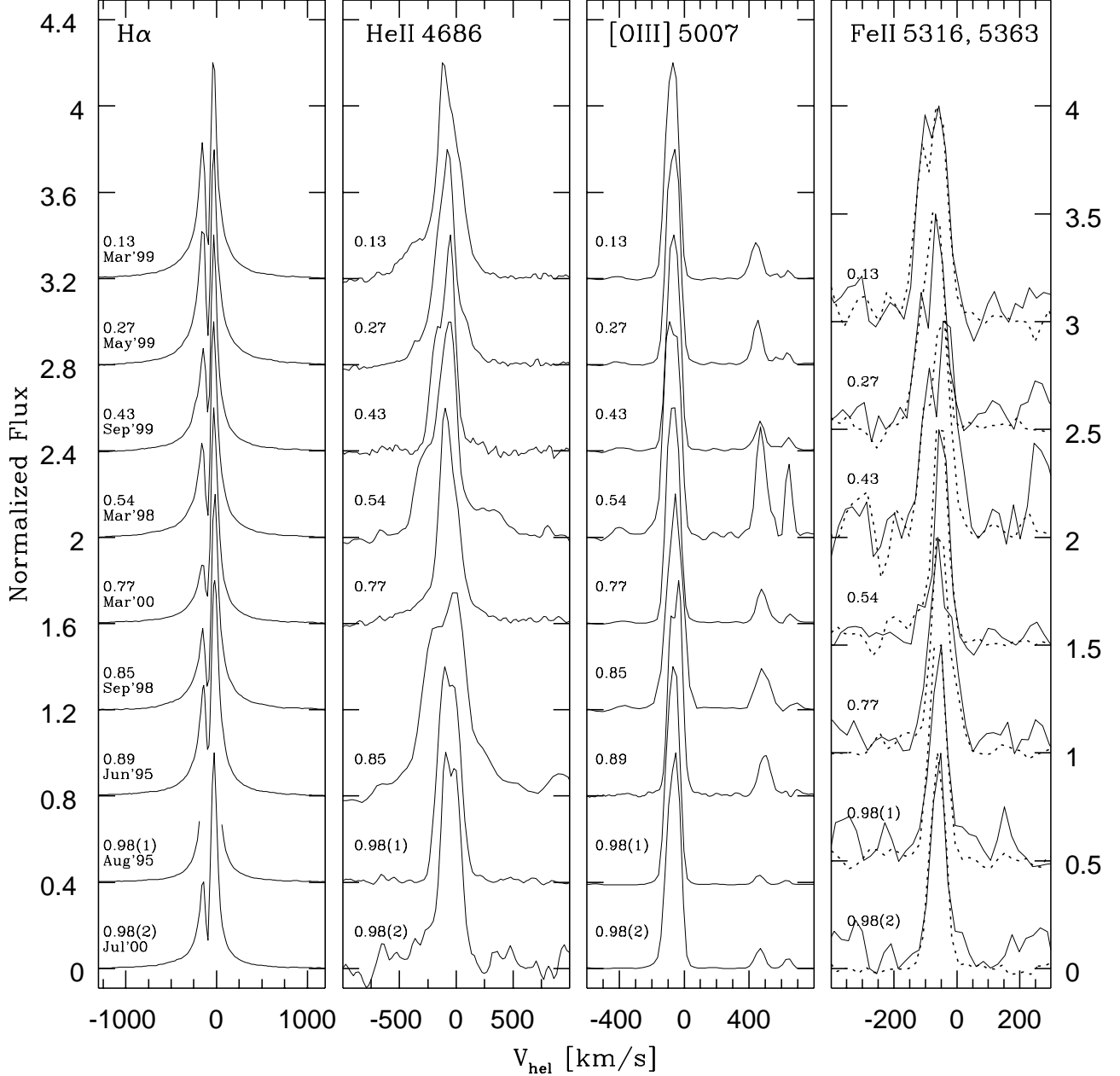


Fig. 1. Emission line profiles in AR Pav. The continuum was subtracted and each profile was normalized to maximum intensity. The profiles are shifted vertically by 0.5 (Fe II) and 0.4 (other lines), respectively, for better display. $H\alpha$ profile corresponding to August 95 is saturated. In the right panel, solid line shows Fe II $\lambda 5316$ and dashed line shows Fe II $\lambda 5363$. Only high resolution spectra are shown.

the relative intensities are similar. The wings are also narrower during eclipse. The double-peaked profiles have an average separation of $117 \pm 3 \text{ km s}^{-1}$, and the average radial velocity of the central absorption is $-90 \pm 2 \text{ km s}^{-1}$.

We have $H\gamma$ profiles only in phases near to both conjunctions. The intensity of the blue peak relative to the red one is smaller than for $H\beta$, except during eclipse. It seems to behave in the same way as $H\alpha$ and $H\beta$. The average radial velocity of the central absorption is $-87 \pm 3 \text{ km s}^{-1}$. The absorption components of the Balmer lines seem to show a positive progression from $H\alpha$ to $H\gamma$. Similar positive progression in radial velocities of the central absorp-

tion component of Balmer emission lines is often observed in symbiotic stars. Since the absorption lines have slower decrement than the emission lines the positive progression may be due to the decreasing effect of the emission border.

The second panel of Fig. 1 shows the He II $\lambda 4686$ emission lines profiles. The line profile is double-peaked during eclipse and in phase 0.85. During eclipse the blue peak is slightly stronger than the red one. In phase 0.85 the red peak is stronger than the blue one. In the rest of the orbital phases they present asymmetric profiles. The asymmetry is reversed in the first quadrature relative to second one. However, in phase 0.13 the shape of the asymmetry

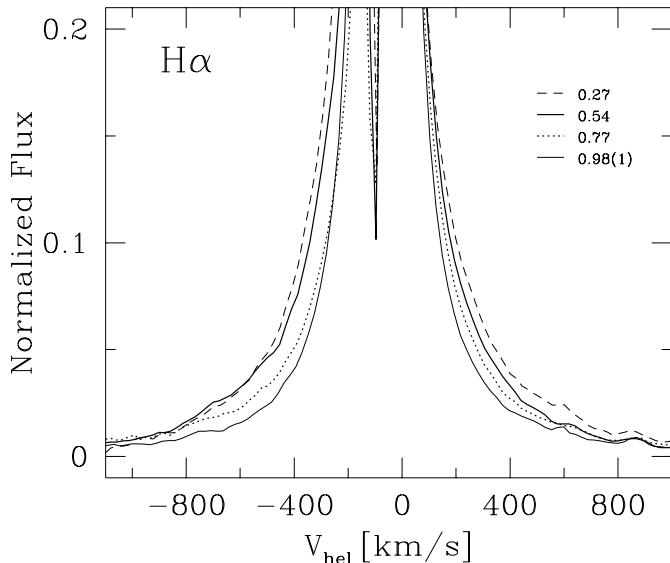


Fig. 2. The wings of H α at selected orbital phases.

is almost identical to phase 0.77. The largest asymmetry occurs in phase 0.54.

Fig. 1 also shows the [O III] λ 5007 emission line region. The permitted lines of He I λ 5016 and Fe II λ 5018 are narrow and more or less symmetric, with FW $\sim 100 - 150 \text{ km s}^{-1}$. The forbidden [O III] lines display FW $\sim 200 \text{ km s}^{-1}$ and may have double peak structure with peak-to-peak separation of $\Delta v \sim 40 \text{ km s}^{-1}$, and the blue to red peak intensity ratio of ~ 1 . This structure is visible in our profiles at phases 0.54 and 0.89 for which we estimate $\Delta v \sim 40$ and 50 km s^{-1} , respectively (Fig. 1), as well as in the profiles presented by van Winckel et al. (1993) and S01.

In the high resolution spectra, also some Fe II emission lines appear as double-peaked and/or asymmetric at most orbital phases (the right panel of Fig. 1). In particular, the profiles are clearly double-peaked near the first quadrature, and asymmetric (with a very weak central absorption occasionally present) at the second quadrature. The profiles seem symmetric and the central reversal is missing during the eclipse whereas at $\phi \sim 0.54$ a very faint blue peak (hardly discernible from the noise) can be present. The double-peaked Fe II profiles have separations between 47 to 65 km s^{-1} . In the spectra of June 1995, the He I emission lines $\lambda\lambda$ 4922, 5876 and 6678 show also a double-peaked profile with an mean separation of 34 km s^{-1} , whereas the He I λ 5016 and the Fe II λ 5018 profiles published by van Winckel et al. (1993) show a reversal at ~ -93 and $\sim -86 \text{ km s}^{-1}$, respectively. It is remarkable that in both conjunctions the intensity of Fe II λ 4923 and λ 5018 emission lines are comparable with the intensities of He I λ 4921 and λ 5015, respectively. In other phases the ratio Fe/He is very small.

3.2. Radial velocities

To obtain the radial velocities of the red giant and the hot component, we have measured spectral features associated with each one.

For the cool component, we have used M-type absorption lines corresponding to Fe I, Ti I, Ni I, Si I, O I, Zr I, Co I, V I, Mg I and Gd II. At some phases we have also identified and measured the blue cF-type absorption lines corresponding to Cr II, Fe II, Ti II and Y II which are believed to be linked to the hot companion (TH74; S01). The individual radial velocities were obtained by a Gaussian fit of the line profile, and a mean value was calculated for each spectrum. The resulting mean heliocentric velocities together with their standard errors and the number of lines used are given in Table 2.

In addition, for the study of the hot component we have determined the radial velocities from the wings of H α , H β and He II λ 4686 profiles. They would reflect the motion of the hot component if they are formed in the inner region of the accretion disk or near to the hot component. In this way we have used a method outlined by Schneider & Young (1980) and Shafter (1983), which was very successful in studies of cataclysmic binaries. This method consists of convolving the data (S) with two identical Gaussian bandpasses (G) whose centers have a separation of $2b$. The wavelength, λ , of an emission line in a spectrum $S(\lambda)$ is given by solving the equation

$$\int_{-\infty}^{+\infty} S(\lambda)G(\lambda - \Lambda)d\lambda = 0$$

where

$$G(x) = \exp[-(x - b)^2/2\sigma^2] - \exp[-(x + b)^2/2\sigma^2].$$

The choice of the parameters b and σ depend on the characteristic of the spectra being analyzed, namely the emission line width and the signal-to-noise ratio of the data. We refer to Shafter (1983) for a more detailed discussion of the influence of the choice of b and σ on the obtained orbital solution. In any case they found that varying these parameters has no significant effect on the resulting value of the system velocity, γ , whereas the semi-amplitude of the radial velocity, K , significantly depends on the choice of b . The resulting velocities are given in Table 2.

In order to reduce the noise in the extreme line wings, we have added all spectra taken in the same observing run. Fig. 1 and Fig. 2 show the H α emission line profiles and wings, respectively, of AR Pav ordered with their orbital phase. We have experimented with a range of values for b , and σ fixed at 7 \AA , for which we have obtained the circular orbit solutions (see below). Fig. 3 illustrates the dependence of the semi-amplitude, K , and its standard error, σ_K on b in the case of H α . It is noticeable that σ_K increases sharply for b larger than $\sim 10 \text{ \AA}$. We can attribute these large standard errors to the velocity measurements dominated by the noise in the continuum rather than by the extreme high velocity wings of the line profile. We have therefore adopted $b = 10 \text{ \AA}$ (460 km s^{-1})

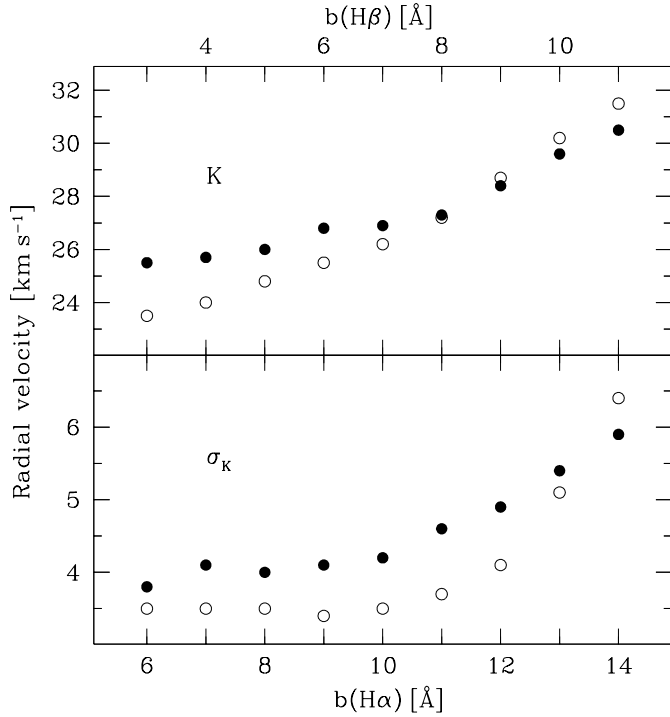


Fig. 3. The orbital semi-amplitude K and its standard error σ_K for the wings of $H\alpha$ (dots) and $H\beta$ (open circles), respectively, as a function of the parameter b . The best estimation of K is determined by the value of b where σ_K begins to sharply increase

as the best value in the case of $H\alpha$. A similar analysis led us to choose $b = 7 \text{ \AA}$ (430 km s^{-1}) and $\sigma = 5 \text{ \AA}$ for $H\beta$, and $b = 5 \text{ \AA}$ (320 km s^{-1}) and $\sigma = 3 \text{ \AA}$ for $He II$, respectively.

We have also obtained the radial velocities of $He I$ $\lambda\lambda$ 4009, 4026, 4121, 4144, 4388, 4471, 4713, 4922, 5016, 5048, 5876, 6678, 7065, 7281; $[O III]$ $\lambda\lambda$ 4363, 4959, 5007; $[N II]$ λ 6584 and occasionally also λ 5755 emission lines as well as numerous $Fe II$ emission lines by a Gaussian fit. Faint $[Fe II]$ though present at some phases have not been measured. Table 2 shows the average heliocentric radial velocities, their errors and number of lines used for each spectrum. The singlet and triplet series of $He I$ lines are shown separately. In the case of double-peaked lines (see above) of $Fe II$ the center velocity were used to derive the values in Table 2.

3.3. Spectroscopic orbits

All radial velocities in Table 2 except the central absorption of $H I$ vary with the 605-day period. Fig. 4 shows our radial velocity data corresponding to the M giant absorption lines, the $H I$ and $He II$ emission wings, and $He I$, $Fe II$, $[O III]$ and $[N II]$ emission lines, respectively, phased with the photometric ephemeris given by Bruch et al. (1994)

$$JD_{Min} = 2420331.3 + 604.5 E.$$

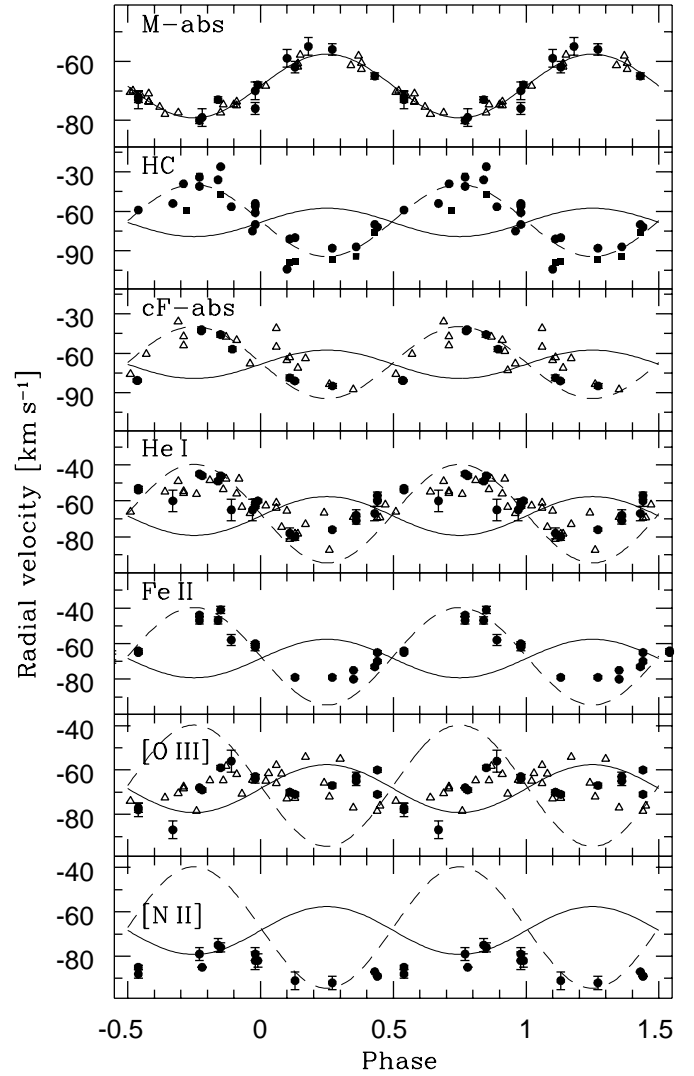


Fig. 4. Radial velocity data and circular orbital solution for AR Pav. Closed symbols represent our data, and triangles represent the data of S01 (M giant) and TH74 (cF absorption and emission lines). The solid line repeats the orbit of the M giant and the dotted line – the hot component solution, respectively (a) M giant absorption. (b) Hot component (HC): filled circles correspond to the $H I$ wings, filled squares correspond to $He II$ λ 4686. (c) cF absorption lines. (d) $He I$ emission lines. (e) $Fe II$ emission lines. (f) $[O III]$ emission lines. (g) $[N II]$ emission lines.

Our radial velocity curve for the M giant is practically indistinguishable from that given by the data from S01 (and also plotted in Fig. 4), and it strongly suggests a circular orbit. It is also obvious from Fig. 4 that the cF absorption system, $H I$ and $He II$ emission wings and the permitted ($He I$ and $Fe II$) emission lines are in antiphase with the M giant absorptions.

In order to obtain the orbital parameters of AR Pav we have assumed a circular orbit as did S01, and adopted the very precise photometric ephemeris of Bruch et al. (1994). The semi-amplitude of the respective radial velocity curve has been then fitted by a least squares method.

Table 2. Radial velocities of the giant absorption lines, the blue cF-type absorption lines, permitted and forbidden emission lines, emission wings of H I and He II lines*, and the central absorption component of H α (HA) in AR Pav

JD/Phase	M-abs	cF-abs	Fe II	He I (s)	He I (t)	[O III]	[N II]	H β	H α	He II	HA
47356 [†] /0.706									-39		-96
47364 [†] /0.719										-60	
48118/0.966				-59 (1)	-68 \pm 9 (2)				-75		
48202/0.105	-59 \pm 3 (5)								-104		
48205/0.110		-79 \pm 2 (9)		-79 \pm 5 (4)	-75 \pm 2 (2)	-70 \pm 1 (2)		-81		-99	
48353/0.355			-75 (1)	-66 \pm 0 (2)	-71 \pm 7 (2)	-63 \pm 2 (2)		-87		-94	
48354/0.356			-80 (1)	-69 \pm 5 (2)	-72 \pm 2 (2)	-65 \pm 2 (2)					
48853/0.182	-55 \pm 3 (9)										
49888/0.894		-57 \pm 2 (9)	-58 \pm 3 (10)	-62 \pm 7 (4)	-71 \pm 13 (2)	-56 \pm 5 (2)	:	-58	-55		-93
49942/0.983	-76 \pm 2 (13)		-61 \pm 1 (34)	-64 \pm 1 (6)	-62 \pm 1 (4)	-64 \pm 2 (3)	-79 \pm 3 (2)	-54	-63	-58	s
50880/0.535	-73 \pm 3 (9)	-81 \pm 1 (40)	-64 \pm 1 (30)	-55 \pm 1 (6)	-52 \pm 2 (4)	-78 \pm 3 (3)	-88 \pm 2 (2)	-57	-61		-105
50881/0.537	-72 \pm 2 (9)	-81 \pm 1 (43)	-65 \pm 1 (32)	-55 \pm 1 (6)	-50 \pm 2 (4)	-77 \pm 2 (3)	-85 \pm 1 (2)				-97
50964/0.674				-60 \pm 9 (5)	-61 \pm 6 (3)	-87 \pm 4 (3)		-54			
51065/0.841	-73 \pm 1 (43)		-47 \pm 2 (10)	-50 \pm 1 (2)	-48 \pm 1 (2)		-75 \pm 3 (2)		-36		-96
51070/0.849		-46 \pm 2 (21)	-41 \pm 2 (24)	-47 \pm 1 (5)	-44 \pm 2 (5)	-59 \pm 1 (3)	-76 \pm 2 (2)	-26		-47	-107
51239/0.129	-62 \pm 2 (13)	-81 \pm 1 (22)	-79 \pm 1 (22)	-81 \pm 2 (5)	-78 \pm 4 (3)	-71 \pm 1 (2)	-91 \pm 4 (2)	-79	-81	-98	-101
51325/0.271	-56 \pm 2 (18)	-85 \pm 2 (14)	-79 \pm 1 (24)	-78 \pm 1 (5)	-74 \pm 3 (4)	-67 \pm 1 (2)	-92 \pm 3 (2)	-91	-85	-96	-90
51423/0.433	-65 \pm 1 (32)		-73 \pm 1 (10)	-72 \pm 2 (2)	-61 \pm 3 (2)		-87 (1)		-70		-99
51424/0.435			-65 \pm 1 (31)	-61 \pm 2 (7)	-51 \pm 3 (4)	-60 \pm 1 (3)	-89 (1)	-72		-76	-86
51425/0.436			-70 \pm 1 (22)	-66 \pm 2 (7)	-61 \pm 4 (4)	-71 \pm 1 (3)	-89 (1)				-100
51629/0.774	-80 \pm 1 (26)	-43 \pm 1 (17)	-44 \pm 1 (29)	-47 \pm 1 (5)	-44 \pm 2 (4)	-68 \pm 0 (2)	-79 \pm 3 (2)	-34	-41	-33	-93
51631/0.778	-79 \pm 3 (21)	-42 \pm 1 (15)	-47 \pm 2 (27)	-48 \pm 1 (5)	-44 \pm 3 (4)	-69 \pm 1 (2)	-85 (1)				-94
51755/0.982	-70 \pm 3 (14)		-60 \pm 1 (33)	-63 \pm 2 (6)	-60 \pm 2 (5)	-63 \pm 1 (3)	-82 \pm 4 (2)	-56	-61	-59	-93
51757/0.986	-68 \pm 1 (66)		-62 \pm 2 (13)	-59 \pm 1 (2)	-61 \pm 2 (2)		-82 \pm 3 (2)				-94

* Sum of the spectra taken in the same observing run.

† Van Winckel(1993)

s: saturated emission

In some cases we have also calculated elliptical orbital solutions with the orbital period forced to the photometric period of 604.5 d. Table 3 lists the resulting orbital solutions. The symbols have their usual meaning: γ is the system velocity, K is the orbital semi-amplitude, e is the eccentricity, ω is the longitude of periastron, T_0 is the time of periastron passage, $f(M)$ is the mass function, $A \sin i$ is the fractional semi-major axis in astronomical units (AU), and ΔT is the time difference between orbital conjunction and photometric eclipse. For the M giant, we have obtained both solutions using only our radial velocities as well as for our radial velocities combined with the S01 data. Although an elliptical orbit fits the measured velocities slightly better than a circular one, the obtained eccentricity $e = 0.12 \pm 0.04$ is only a 3σ result, and observations covering several more orbital periods would be necessary to confirm the reality of such an orbit. Following the arguments given by S01 we believe that a circular orbit provides a better description of the data, and such an orbit is also in agreement with the tidal theory.

Both the broad emission line wings, and the cF-type absorption lines show the highest (and practically the same) amplitude and the mean velocity almost identical with the red giant systemic velocity. The solutions for the broad emission wings of H I and He II, respectively,

agree within their respective errors which suggests that both they are formed in the same region near the hot component. An A- or F-type absorption system with radial velocity varying in antiphase with the M giant absorption lines, similar to that identified in AR Pav, was seen during outbursts of two other symbiotic systems AX Per and BX Mon, and associated with the hot component (Mikołajewska & Kenyon 1992a, Dumm et al. 1998). This combined with the fact that the wings narrow during the hot component eclipse strongly suggests that both the broad emission wings and the blue (cF) absorption system trace the orbit of the hot component. The only problem is that any orbital solution for the cF absorption system leads to significant eccentricity (Table 3; TH74; S01) whereas the red giant orbit requires a circular (or nearly circular) orbit for the hot companion. Our orbital solution for the broad emission line wings, on the other hand, is consistent with a circular orbit.

To analyze the cF absorption system we have combined our measurements with the TH74 data. Since our measurements are a factor of 2-4 more accurate than those of TH74, we have applied a weight 4 to our data, and weights 1-3 to the TH74 data (same as in their Table 1), respectively. We have re-calculated the orbital solution for the combined data and found practically the same eccen-

Table 3. Orbital solutions for AR Pav

Component	γ [km s ⁻¹]	K [km s ⁻¹]	e	ω	$T_0^{(1)}$	$f(M)$ [M_\odot]	$A \sin i$ [AU]	$\Delta T^{(2)}$
M abs (our)	-68.3 ± 0.8	11.4 ± 1.2	$0^{(3)}$					
M (our+S01)	-68.4 ± 0.3	10.8 ± 0.5	$0^{(3)}$			0.079 ± 0.011	0.60 ± 0.03	$0^{(3)}$
M (our+S01) ⁽⁴⁾	-68.2 ± 0.2	10.9 ± 0.4	0.12 ± 0.04	351 ± 12	50693 ± 20	0.079 ± 0.009	0.60 ± 0.02	12
cF (our+TH74) ⁽⁵⁾	-66.5 ± 1.3	27.6 ± 2.9	0.45 ± 0.07	273 ± 11	50899 ± 21	0.94 ± 0.40	1.37 ± 0.19	34
cF (our+TH74) ⁽⁶⁾	-67.4 ± 1.1	22.8 ± 1.7	0.21 ± 0.07	307 ± 20	50936 ± 31	0.69 ± 0.18	1.23 ± 0.11	4
Wings (H I)	-65.2 ± 1.9	26.3 ± 2.7	$0^{(3)}$			1.14 ± 0.32	1.48 ± 0.15	$0^{(3)}$
Wings (H I) ⁽⁴⁾	-64.8 ± 1.4	25.8 ± 1.8	0.13 ± 0.07	68 ± 29	51726 ± 45	1.05 ± 0.26	1.42 ± 0.12	-7
Wings (He II)	-70.4 ± 2.7	28.9 ± 3.9	$0^{(3)}$			1.51 ± 0.70	1.60 ± 0.22	$0^{(3)}$
Wings (H I+He II)	-67.1 ± 1.6	27.4 ± 2.3	$0^{(3)}$			1.29 ± 0.35	1.52 ± 0.13	$0^{(3)}$
He I	-63.3 ± 1.8	15.0 ± 2.8	$0^{(3)}$					$0^{(3)}$
He I (s)	-64.2 ± 1.8	15.6 ± 2.8	$0^{(3)}$					$0^{(3)}$
He I (t)	-62.2 ± 2.0	14.1 ± 3.1	$0^{(3)}$					$0^{(3)}$
Fe II	-63.6 ± 0.9	17.8 ± 1.4	$0^{(3)}$					$0^{(3)}$

(1) the time of periastron passage;

(2) $\Delta T = T_{\text{conj}} - T_{\text{eclipse}}$;

(3) assumed;

(4) unconstrained solution;

(5) unconstrained, weighted solution;

(6) same as (5) for quiescent data only (see text).

tricity, $e = 0.45 \pm 0.07$, as $e \sim 0.45$ and 0.42 given by TH74 and S01, respectively, and $\gamma = -66.5 \text{ km s}^{-1}$, closer to the red giant systemic velocity than earlier solutions. The spectroscopic conjunction occurs 34 days after the photometric eclipse. S01 suggested that the cF absorption system only traces the hot component's motion whilst it is in front of the giant. At other orbital phases, the cF absorption lines are affected by additional absorption due to this wind and/or a flow of material towards the hot companion, and the resulting radial velocities mimics an elliptical orbit. S01 have also demonstrated that a circular orbit that is almost exactly in antiphase with the red giant results if only the radial velocity measurements between phase 0.25 and 0.75 (the hot component in front) are employed. Unfortunately, our new measurements, in particular 2 points almost coincident at phase ~ 0.5 do not fit this restricted orbital solution of S01. Instead we have found that the cF absorptions may be affected by the hot component activity. This is illustrated in Fig. 5. In particular, all data points that force an elliptical orbit – the TH74 points between phase ~ 0 and 0.2 as well as our two points near phase ~ 0.5 – were obtained when AR Pav was very active (TH74; Skopal et al. 2000b). It is interesting that an orbital solution omitting the TH74 data from the 1954 outburst as well as our measurements obtained prior to JD ~ 2451000 (when according to Skopal et al. (2000b) AR Pav was very active) results in a much lower eccentricity, $e = 0.21 \pm 0.07$ and the spectroscopic conjunction at the time of the photometric eclipse. Both these fits, however, match the data rather poorly, and the residuals for some points are larger than their measurement accuracy. This illustrates difficulties with interpretation of the radial velocity curve of the blue absorption system.

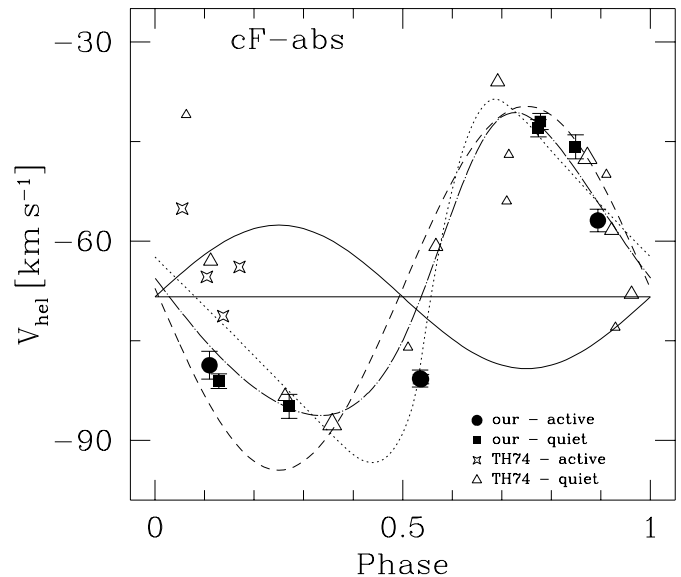


Fig. 5. The radial velocity curve for the cF shell component with our circular orbits of the red giant (solid curve) and the broad emission wings (dashed curve), respectively. The horizontal line represents the system velocity, $\gamma = -68.4 \text{ km s}^{-1}$. Open symbols (triangles and stars) represent the TH74 data, with sizes reflecting their weights. Filled symbols (squares and dots) correspond to this work. We use different symbols for data obtained during activity and quiescence, respectively. The dotted curve gives an elliptical fit to all data points, the dot-dashed curve – to quiescent data only.

We note here that similar complications with the blue absorption system occurred for a few other active symbi-

otic systems. In the case of symbiotic recurrent nova RS Oph, Dobrzycka & Kenyon (1994) found the A-type absorption features $\sim 0.4 P$ out of phase with the orbit of the giant. Mikołajewska & Kenyon (1996) failed to derive any radial velocity curve and orbital solution for the blue absorption system in Z And, whereas in CI Cyg the radial velocities of the F-type absorption system suggest formation region in material streaming from the giant near the hot component (Mikołajewska & Mikołajewski 1988).

Such problems are also common in the case of W Ser stars (or hyperactive Algols), in which the accreting primary is embedded in an optically thick shell with an A/F-type spectrum, and strong emission from circumstellar plasma is also present. We recall here that the radial velocity curves for the shell spectra in W Ser stars show often significant departure from that expected for a circular orbit required by the orbital solutions for their secondary components (Andersen et al. 1988). It has been also found that such significant departures can be expected if the shell lines used to measure the radial velocity curve are formed in the outer 10 – 20 % of the disk (e.g. Andersen et al. 1988). In particular, the distorted radial velocity curve of the shell in SX Cas (Fig. 1 of Andersen et al. 1988) is very similar to the radial velocity curve of the blue absorption system in AR Pav.

The possible correlation between AR Pav’s activity and the departures of the cF absorption velocities from the circular orbit suggests that this absorption system may be also affected by material streaming towards the hot component presumably in a region where the stream encounters an accretion disk or an extended envelope around the hot component. The outer disk and the stream impact region can be highly unstable and asymmetric. For example, the trailing side of the disk, where the gas stream adds to the disk, can be brighter whereas the leading side is more extended. Such asymmetry may, at least qualitatively, account for the deviations of the cF absorption velocity curve from the sinusoid expected for a circular orbit as well as for the behaviour of the optical light curves of AR Pav, which show relatively stable profile of eclipses during quiescence in contrast to very unstable profiles and changes in the position of the minima during activity (Andrews 1974; Bruch et al. 1994; Skopal et al. 2000a).

Unfortunately, a detailed and proper treatment of the cF shell radial velocity curve is beyond the scope of our paper. This would require knowledge of the temperature and density profile in the shell/disk which is not available. The situation is further complicated by significant cycle-to-cycle variations of the cF spectrum. In particular, spectroscopic observations a few orbital cycles and of good phase coverage in each cycle are necessary to distinguish between the cycle-to-cycle changes of the radial velocity curve and distortions due to other effects (e.g. contribution from stream, formation in outer disk, etc.).

The solutions for the broad emission line wings are free from such complications and they are not affected by the system activity. We thus believe that the broad wings are formed very close to the hot star (in the inner disk or in

a hot wind) and they directly trace the hot component’s orbit.

Combing the semi-amplitudes of the M giant and the H I+He II emission line wings for the circular orbit (Table 3) gives a mass ratio $q = 2.5 \pm 0.3$, and component masses of $M_g \sin^3 i = 2.5 \pm 0.6 M_\odot$ and $M_h \sin^3 i = 1.0 \pm 0.2 M_\odot$, with the errors given by the errors of the K_h and K_g values, respectively. These values are somewhat larger than $M_g \sin^3 i = 1.9 M_\odot$ and $M_h \sin^3 i = 0.75 M_\odot$ derived by S01 mostly because our semi-amplitude for the M giant, $K_g = 10.8 \text{ km s}^{-1}$, is larger than the value $K_g = 9.6 \text{ km s}^{-1}$ calculated by S01. We, however, note that our radial velocity curve (Figure 4) has better coverage at both quadratures.

The radial velocities of the central absorption component of H I Balmer lines do not follow the orbital phase, and are blueshifted by $\sim 30 \text{ km s}^{-1}$ relative to the system velocity. The absorption is presumably formed in the neutral portion of the cool component’s wind. Moreover, it remains strong and practically constant over whole orbital cycle, which indicates that the nebula in AR Pav is probably bounded on all sides by significant amount of neutral material at least near the orbital plane. It is interesting that most symbiotic systems with double-peaked H α profiles have the main reversal on the blue side of the line center, strongly supporting the idea that this structure arises from self-absorption in the cool giant’s wind (Iverson et al. 1994).

For a weak, unsaturated absorption the relationship between column density, N_i , and the measured equivalent width, EW , is

$$N_i = \frac{1.13 \times 10^{20} EW}{\lambda^2 f_{ij}} \text{ cm}^{-2},$$

where f_{ij} is the oscillator strength of the transition $i \rightarrow j$, and wavelength λ and EW are given in \AA . From the measured $EW(\text{H}\alpha) = 1.17 \pm 0.03 \text{ \AA}$, we estimate the lower limit for $N(\text{H I}, n = 2) \gtrsim 4.4 \times 10^{12}$, and from $EW(\text{H}\beta) = 0.66 \pm 0.06 \text{ \AA}$ we obtain $N(\text{H I}, n = 2) \gtrsim 3 \times 10^{13} \text{ cm}^{-2}$, respectively. To estimate the total hydrogen column density, $N(\text{H})$, the concentration of hydrogen atoms at the second excitation level has to be adopted which requires detailed knowledge on physical conditions in the gas. Assuming local thermodynamic equilibrium (LTE) and a temperature, $\lesssim 6000 \text{ K}$, we obtain (from the Saha-Boltzman relation) $N(\text{H I}, n = 2)/N(\text{H}) \lesssim 10^{-8}$, and the total hydrogen column density $N(\text{H}) \gtrsim \text{a few} \times 10^{21} \text{ cm}^{-2}$. Despite of all uncertainties involved in this estimate, the resulting hydrogen column density is consistent with the behavior of the shortwavelength IUE spectra of AR Pav. These spectra show characteristic attenuation of the continuum flux for $\lambda \lesssim 1500 \text{ \AA}$ at any phase – including SWP 5828 and SWP 13956 taken at orbital phases 0.27 and 0.37, respectively – which can be accounted for by Rayleigh scattering in the neutral material surrounding the binary system. It has been shown that to produce a noticeable effect column densities in the range $N(\text{H I}) \sim 10^{20} - 10^{24} \text{ cm}^{-2}$ are required (e.g. Schmid 1997). We thus conclude that both

the strength of the central absorption in H I Balmer lines and the behavior of the IUE SWP spectra are consistent with significant amounts of neutral material bounding the nebula in the orbital plane.

The radial velocity curves for He I and Fe II emission lines are in antiphase with the cool giant, which suggests a possible association of these lines with the hot component. However, their semi-amplitude, ~ 15 and $\sim 18 \text{ km s}^{-1}$ for He I and Fe II, respectively, are a factor of ~ 2 lower than that of the hot component, and their mean velocities are redshifted by $\sim 5 \text{ km s}^{-1}$ with respect to the system velocity. Such discrepant amplitudes can be explained by a contribution from material between the two stars and in the neighborhood of the red giant which can both reduce the amplitude and shift the mean velocity (see also discussion in S01). We have not found any significant difference between the K values as well as γ velocity derived for the singlet and triplet He I emission series, respectively. There is also no difference between our radial velocity curve and the data from TH74, which means that the He I formation region was the same at the two epochs.

The radial velocities of the forbidden lines show a more complicated pattern (Fig. 4, bottom). The [O III] emission lines do not trace any of the two stellar components. Our radial velocity data show a deep minimum around the phase ~ 0.7 and another less marked minimum around the phase ~ 0.2 , and the mean velocity, -68 km s^{-1} , very close to our red giant γ velocity. A small amplitude periodic RV changes are also present in TH74 data. S01 suggested that the variability may be due to variable relative size of the blue and red peaks causing the line center of unresolved [O III] lines (such as [O III] $\lambda 4363$ in TH74) to move bluewards and redwards. However, we have found the same RV values and changes by measuring the line centers and the wings, respectively, which in our opinion suggests that the changes are due to true motions.

Finally, the [N II] emission lines show a small periodic changes roughly in phase with the hot component and the mean velocity blueshifted by $\sim 16 \text{ km s}^{-1}$.

3.4. The M giant, the hot companion and the geometry of AR Pav system

AR Pav is well-established eclipsing system. The eclipses are however not total as indicated by relatively blue colours during mid-eclipse, $B - V \sim 0.6$, much different from $B - V \sim 1.5$ expected for an M5 giant, and variable UBV magnitudes during minimum which increase with the magnitudes outside eclipse (Andrews 1974; Hutchings et al. 1983). Similarly, the UV continuum flux measured from IUE spectra (cf. Fig. 5 of S01) shows a significant reduction near $\phi = 0$, the continuum is, however, not fully eclipsed, and the shape of the light curve is asymmetric and complex. S01 estimated a limit $i \gtrsim 79^\circ$ from the observed exit from eclipse for a point-like source and using the red giant radius derived from its rotational velocity.

An independent estimate of the orbital inclination can be made by comparing the apparent red giant radius inferred from eclipses, $R_{g,\text{ecl}}$, with its mean tidal radius, R_t , defined as the radius of a sphere with a volume equal to the Roche lobe volume. The inclination is

$$\cos i \leq \sqrt{(R_t/A)^2 - (R_{g,\text{ecl}}/A)^2}.$$

Skopal et al. (2000a) obtained $R_{g,\text{ecl}}/A = 0.30 \pm 0.02^2$, while $R_t/A = 0.46 \pm 0.01$ for $q = 2.5 \pm 0.3$ (Paczynski 1971). If the giant actually fills its tidal lobe, the orbital inclination is $i = 70^\circ \pm 2^\circ$, so $M_g \sim 3 M_\odot$ and $M_h \sim 1.2 M_\odot$. Otherwise these estimates give a strong lower limit for i and upper limits for the binary component masses.

Our orbital solution yields a binary separation of $A \sin i = 457 \pm 35 R_\odot$. For $i = 90^\circ$, the giant radius derived from eclipses is then $0.3A = 137 \pm 20 R_\odot$, very close to the value $130 \pm 25 R_\odot$ derived by S01 from rotational velocity. The red giant radius extends to $\gtrsim 65\%$ of the mean Roche lobe radius³ with the lower limit set by $i = 90^\circ$. Based on similar estimate for the Roche lobe filling factor S01 concluded that the giant in AR Pav does not fill its tidal lobe. In our opinion, however, this result does not settle the problem.

Recently, Orosz & Hauschildt (2000) have shown that rotational broadening kernels for Roche lobe filling (or nearly filling) giants can be significantly different from analytic kernels due to a combination of the nonspherical shape of the giant and the radial departure from a simple limb darkening law. As a result, geometrical information inferred from $v \sin i$ measurements of cool giants in binary systems, and in particular in symbiotic stars, are likely biased and must be treated with caution. In particular, among symbiotic systems with measured $v \sin i$ and accurate orbits, three of them, T CrB, CI Cyg and BF Cyg, seem to contain tidally distorted giants as indicated by their red/near-IR light curves with evident ellipsoidal changes (Belczyński & Mikołajewska 1998; Mikołajewska 2001; Mikołajewska et al. 2002). In CI Cyg, the rotational velocity of the giant is consistent with a synchronously rotating Roche lobe filling giant (Kenyon et al. 1991). In T CrB, however, the observed $v \sin i$ is by $\sim 20 - 30\%$ lower than expected for such a giant (Belczyński & Mikołajewska 1998). A very low $v \sin i = 4.5 \pm 2 \text{ km s}^{-1}$ has been also measured for the red giant in BF Cyg (Fekel et al. 2001). The problem is further complicated by the fact that the ellipsoidal variations can be hardly visible only in quiescent visual light curves, whereas systematic searches for such changes in the red and near-IR range where the cool giant dominates the continuum light are missing (Mikołajewska 2001). In

² Note that this estimate is based only on the shape of light curve and it is independent of the model adopted in their paper.

³ The ratio of the observed red giant's radius to the mean tidal radius, R_t is a better measure of the Roche lobe filling factor than the ratio of the giant's radius to the distance of the inner Lagrange point from the giant's center adopted by S01.

fact, a secondary minimum is also visible in the quiescent optical light curves of AR Pav (Fig.1 of Skopal et al. 2000a). Observations in the red and near-IR range are, however, necessary to confirm whether this minimum is due to ellipsoidal changes of tidally distorted red giant.

Based on near IR TiO band depths, Mürset & Schmid (1999) estimated a spectral type M5 III for the giant, whereas Allen (1980) deduced M6 III from the 2.3- μm CO band. If the giant is similar to normal giants, then its effective temperature should be between $T_{eff}(\text{M5 III}) = 3355$ K and $T_{eff}(\text{M6 III}) = 3240$ K (Richichi et al. 1999), and luminosity, $L_g \sim 1800 - 4700 L_\odot$, for $R_g = 130 R_\odot$ and $R_g = R_t = 210 R_\odot$, respectively. Comparing the position of the red giant in the HR diagram with the evolutionary tracks for RGB/AGB stars, we find the red giant's mass range of $2 M_\odot \lesssim M \lesssim 5 M_\odot$ (e.g. Vassiliadis & Wood 1993; Schaller et al. 1992; Bessel et al. 1989), consistent with our dynamical mass estimate.

The radial velocity curve of the F-type absorption lines suggest that the shell spectrum is formed in the outermost accretion disk and/or the region where the stream encounters the inner accretion disk or an extended envelope around the hot component. The broad emission wings could be then formed in the inner accretion disk or the extended envelope around the hot source. TH74 came to similar conclusion based on the radial velocity behavior and the fact that the Balmer continuum served as a strong background for the cF absorption lines. We can place some limit on the size of the inner disk radius assuming Keplerian rotation. Then we have

$$R_d/R_\odot \approx 19 \times (M_h/M_\odot)(v_d/100 \text{ km s}^{-1})^{-2} \sin^2 i.$$

In particular, the $\text{H}\alpha$ line wings follow the hot companion's orbit down to at least $\pm 270 \text{ km s}^{-1}$ ($b \gtrsim 6 \text{ \AA}$; Fig. 3), which corresponds to a Keplerian disk radius of 2.6 and $2.8 R_\odot$, for $i = 90^\circ$ and 70° , respectively. These values are much lower than the radius of the eclipsed object, $R_{h,ecl} \sim 0.1 A (46 R_\odot)$, derived from optical eclipses (Skopal et al. 2000a; Andrews 1974). Unfortunately, our method does not allow to measure accurately the wing positions for $b \lesssim 6 \text{ \AA}$ because of the presence of strong central absorption. We also note, that the projected Keplerian velocity at an outer disk rim with $R_d \sim 46 R_\odot$ is $\sim 128 \text{ km s}^{-1}$, very close to the average peak-to-peak separation in Balmer lines, ~ 148 for $\text{H}\alpha$ and $\sim 117 \text{ km s}^{-1}$ for $\text{H}\beta$, respectively. However neither the two peaks nor the central absorption trace the hot component orbital motion (see also Sec. 3.3). Thus we do not believe that the observed double-peaked structure originates in an outer accretion disk.

The maximum velocity in the $\text{H}\alpha$ line profile, $\gtrsim 800 \text{ km s}^{-1}$, is consistent with a Keplerian velocity at a distance of $\lesssim 0.3 R_\odot$, which sets an upper limit for the radius of the hot component. Although this value is an order of magnitude larger than the expected radius of a $1 M_\odot$ white dwarf, it falls in the range of the observed hot component radii in classical symbiotic systems (e.g. Mürset et al. 1991). This result also rules out the presence of a main-sequence accretor in AR Pav.

The permanent presence of the strong central absorption in H I Balmer emission lines, stationary with respect to the orbital motion, indicates that the nebula is bounded on all sides by significant amount of neutral material (see Sec. 3.3). On the other hand, the strong double-peaked [O III] lines require an extended low-density ionized region. A plausible solution to this apparent inconsistency is a bipolar ionization structure of the nebula, with a lower density towards the poles than in the orbital plane. We note here that similar strong [O III] lines together with strong central absorption in H I emission lines were observed during late outburst phases and decline in CI Cyg and AX Per. Moreover, in AR Pav, the eclipses in H I and He II lines are narrow with well-defined eclipse contacts (TH74; Quiroga et al., in preparation) likewise the eclipses in CI Cyg and AX Per during the outburst and its decline (Mikołajewska & Kenyon 1992a, 1992b) which indicates that they may arise in a non-spherical, perhaps bipolar, nebula or flow. Such a geometry is also consistent with the recent radio observations of CI Cyg (Mikołajewska & Ivison 2001). These bipolar structures could be associated with the presence of an accretion disk in AR Pav and related symbiotic systems at least during their active phases.

Even if the giant does not fill its Roche lobe, its wind is likely focused towards the secondary and/or towards the orbital plane (Mastrodemos & Morris 1998, 1999; Gawryszczak, Mikołajewska & Różycka 2002). In particular, 3-D hydrodynamic model calculations show that, in a system with orbital parameters similar to those of AR Pav, gravitational interaction of the cool giant's with the secondary all alone can produce an equatorial to polar density contrast as large as 100-1000 giving rise to a bipolar geometry of the circumstellar nebula even in the absence of an accretion disk.

A bipolar geometry of the nebula of AR Pav can also account for the orbital phase-dependent changes of the [O III] and [N II] emission lines. In particular, such variations can be expected if these lines are formed in the hot component wind confined by the asymmetric dense wind from the red giant or in the wind-wind interaction zone (e.g. Walder & Follini 2000). The radial velocity curves for the [O III] and [N II] emission lines, respectively, are not in phase, presumably because the two ions probe different regions, in particular with different density (note that the forbidden line emission is the most effective if the electron density is near to the respective critical density).

4. Concluding remarks

We have obtained the circular orbits for both components of AR Pav from direct radial velocity measurements of the M-giant and the hot component. In particular, we have found that the hot component orbital motion can be successfully traced by radial velocities derived from the broad emission wings of H I Balmer lines and He II lines. Similar result has been recently obtained by Ikeda & Tamura (2000; also Fekel et al. 2001) for V1329 Cyg, in which the H I and He II broad wings appear to fol-

low the hot component orbit. With both radial velocity curves, we have obtained the orbital parameters and dynamical masses for each component. The masses obtained are $M_g \sin^3 i = 2.5 \pm 0.6 M_\odot$ and $M_h \sin^3 i = 1.0 \pm 0.2 M_\odot$ for the red giant and the hot component respectively.

Our M-giant orbit is in good agreement with that given by S01. We believe that the somewhat higher semi-amplitude derived from combined our and S01 velocity data results from a better coverage of the final radial velocity curve near its minimum and maximum. Our improved mass function, $f(M_g) = 0.079 M_\odot$, combined with the red giant's mass, $M_g = 2.0 M_\odot$, derived by S01 from evolutionary tracks yields $M_h = 0.87 M_\odot$, in agreement with our dynamical mass estimate. As in S01, our final component masses are very different from earlier published values (TH74; Skopal et al. 2000a). In particular, our upper limit for the hot component mass, $M_h \lesssim 1.2 M_\odot$, is much lower than the $2.5 M_\odot$ and $4.5 M_\odot$ values found by TH74 and Skopal et al., respectively, and it does not require the presence of a main-sequence companion to the M giant. Moreover, our analysis (Sec. 3.4) practically rules out such possibility. Instead, we find that the hot component, like in most symbiotic stars, resembles central stars of planetary nebulae. However, we must stress that the hot component of AR Pav seems to be one of the most massive among thusfar studied symbiotic systems.

AR Pav is also one of the most active symbiotic systems. In particular, its optical light curve in addition to eclipses shows strong cycle-to-cycle variability (e.g. Andrews 1974; Bruch et al. 1994; Skopal et al. 2000a) which is related to the presence and strength of the cF absorption spectrum and a blue continuum (TH74; Hutchings et al. 1983). Such a blue A/F-type shell spectrum is typical for symbiotic systems during outbursts (active phases), in particular for those with multiple Z And-type eruptions, and it seems to be associated with the hot component (Mikołajewska & Kenyon 1992a, 1992b). Usually, the blue shell component disappears during a few years after the visual maximum, and a typical symbiotic system spends more time in quiescence than in activity (Mikołajewska & Kenyon 1992a). In the case of AR Pav however the F-type component remained visible, although weakened following the decline of the optical brightness, throughout all the period 1953-1973 covered by the observations of TH74, as well as during our observations in 1990-2000. Moreover, a warm blue continuum was also present in 1980-1982 (e.g. Hutchings et al. 1983); unfortunately there are not published optical spectra which could confirm the presence of any blue absorption system. Thus, the hot component of AR Pav, unlike the hot components in typical symbiotic systems, seems to remain active most of time. There is also rather no doubt that this high activity is somehow related to variable accretion processes.

Finally, AR Pav shares many properties with W Ser stars (or hyperactive Algols). In particular, both seem to have the accreting star embedded in an optically thick shell with an A/F-type spectrum, and strong emission from circumstellar plasma. In the case of W Ser

stars, there is strong evidence that the shell spectrum is formed mainly in a geometrically and optically thick accretion disk seen nearly edge-on and in a gas stream (e.g. Andersen et al. 1988 and references therein). Kenyon & Webbink (1984) propose the same interpretation for the A/F-type shell spectrum observed in AR Pav, CI Cyg and a few other symbiotic systems during their active phases. Our analysis of radial velocity patterns in the F-type shell absorption as well as various emission lines in AR Pav supports such interpretation. The main difference between these symbiotic systems and W Ser stars is that the He II recombination lines, such as $\lambda 1640 \text{ \AA}$ and $\lambda 4686 \text{ \AA}$ are absent in W Ser stars whereas they are strong in AR Pav, CI Cyg and other related symbiotic stars (except during the maximum of the strongest optical outbursts). This seems to be related to different nature of the accretor hidden inside the disk, which in W Ser stars seems to be a main-sequence B-type star whereas in AR Pav and other symbiotics the accretor is less massive, $M_h \lesssim 1 M_\odot$, much hotter, and perhaps more compact. Both AR Pav and W Ser stars also have very complex and variable light curves, which can be accounted for by instabilities of a luminous disk component, and/or variations in mass transfer and circumstellar gas in the system. A complex circumstellar envelope is also suggested by variable polarization in both AR Pav and W Ser stars (Brandi et al. 2000 and Plavec 1980, respectively).

Although it is very premature to claim that all symbiotic systems with multiple outburst activity do have tidally distorted giants, and – at least during active phase – accretion disks, whereas the non-eruptive systems do not, the former seems to be the case for CI Cyg, YY Her, and a few other active systems. The latter is also true in the case of two non-eruptive systems, V443 Her and RW Hya, which do not show any evidence for ellipsoidal variability in their near-IR light curves, and their near-IR magnitudes show only small fluctuations with the observational errors (Mikołajewska et al. 2002).

AR Pav certainly deserves further studies. For example, near infrared monitoring can provide important information about the process of mass transfer and accretion by confirming or excluding a tidally distorted giant. The structure of the nebula and the hot continuum source may be reconstructed and tested during the eclipses. AR Pav has not yet been detected in radio range, and the available upper limit $F_{6 \text{ cm}} \lesssim 14 \text{ mJy}$ (Belczyński et al. 2000) is very far from the present detection limits. Multifrequency radio observations would give us information about the mass loss and the geometry of ionized region. We also desperately need good models of the structure and spectra of accretion disks and boundary layers for symbiotic stars.

Acknowledgements. CQ is grateful to Nicolaus Copernicus Astronomical Center for hospitality and support during the partial preparation of this paper. We thank Nidia Morrell for the acquisition of the 1999 May image. We wish to acknowledge the facilities and support offered by the staff of the CASLEO. We also thank the anonymous referee for valuable remarks and suggestions. This research was partly

supported by KBN research grants No. 2P03D 021 12 and No. 5P03D 019 20.

References

- Allen, A. D. 1980, *MNRAS*, 192, 531
- Andersen, J., Nordström, B., Mayor, M., Polidan, R.S. 1988, *A&A* 207, 37
- Andrews, P. J. 1974, *MNRAS*, 167, 635
- Baldwin, J. A., Stone, R. P. S. 1984, *MNRAS*, 206, 241
- Barbá, R., Brandi, E., García, L., Ferrer, O. 1992, *PASP*, 104, 330
- Belczyński, K., Mikołajewska, J. 1998, *MNRAS*, 296, 77
- Belczyński, K., Mikołajewska, J., Munari, U., Friedjung, M. 2000, *A&AS* 146, 407
- Bessell, M. S., Brett, J. M.; Wood, P. R., Scholz, M. 1989, *A&AS*, 77, 1
- Brandi, E., Garcia, L.G., Piirola, V., Scaltriti, F., Quiroga, C. 2000, *A&AS*, 145, 197
- Bruch, A., Niehues, M., Jones, A.F. 1994 *A&A*, 287, 829
- Dobrzycka, D., Kenyon, S.J. 1994, *AJ* 108, 2259
- Dumm, T., Mürset, U., Nussbaumer H., et al. 1998, *A&A*, 336, 637.
- Fekel, F.C., Hinkle, K.H., Joyce, R.R., Skrutskie, M.F. 2001, *AJ*, 121, 2219
- Gawryszczak, A.J., Mikołajewska, J., Różyńska, M. 2002, *A&A*, in press
- Hutchings, J.B., Cowley, A.P., Ake, T.B., Imhoff, C.L. 1983, *ApJ*, 275, 271
- Ikeda, Y., Tamura, S. 2000, *PASJ*, 52, 589
- Iverson, R.J., Bode, M.F., Meaburn, J. 1994, *A&AS*, 103, 201
- Kenyon, S.J., Webbink, R.F. 1984, *ApJ*, 279, 252
- Kenyon, S.J., Oliverson, N.A., Mikołajewska, J., et al. 1991, *AJ*, 101, 637
- Mastromedemos, N., Morris, M. 1998, *ApJ*, 497, 303
- Mastromedemos, N., Morris, M. 1999, *ApJ*, 523, 357
- Mayall, M. W. 1937, *Ann. Harv. Coll. Obs.*, 105, 49 1
- Mikołajewska, J. 2001, in *Small-Telescope Astronomy on Global Scales*, ed. B. Paczyński, W.P. Chen, & C. Lemme, *ASP Conf. Ser.*, 246, 167/astro-ph/0103496
- Mikołajewska, J., Iverson, R.J. 2001, *MNRAS*, 324, 1023
- Mikołajewska, J., Kenyon, S. J. 1992a, *AJ*, 103, 579
- Mikołajewska, J., Kenyon, S. J. 1992b, *MNRAS*, 256, 177
- Mikołajewska, J., Kenyon, S. J. 1996, *AJ*, 112, 1659
- Mikołajewska, J., Mikołajewski, M. 1988, in *The Symbiotic Phenomenon*, ed. J. Mikołajewska et al. (Kluwer, Dordrecht) 187
- Mikołajewska, J., Kolotilov, E.A., Shenavrin, V.I., Yudin, B.F. 2002, in *B.T. Gansicke, K. Beuermann, K. Reinsch, eds, The Physics of Cataclysmic Variables and Related Objects*, *ASP Conf. Ser.*, in press
- Mürset, U., Schmid, H. M. 1999, *A&AS*, 137, 473
- Mürset, U., Nussbaumer, H., Schmid, H. M., Vogel, M. 1991, *A&A*, 248, 458
- Orosz, J.A., Hauschildt, P.H. 2000, *A&A*, 364, 265
- Paczyński, B. 1971, *ARA&A*, 9, 183
- Plavec, M. J. 1980, in *IAU Symp. 88, Close Binary Stars: Observations and Interpretation*, eds: M. J. Plavec, D. M. Popper and R. K. Ulrich (Reidel), 251
- Richichi, A., Fabbroni, L., Ragland, S., Scholz, M. 1999, *A&A*, 344, 511
- Schaller, G., Schaerer, D., Meynet G., Maeder, A. 1992, *A&AS*, 96, 269
- Schmid, H.M., 1997, in *Physical processes in symbiotic binaries*, ed. J. Mikołajewska (Copernicus Found. for Polish Astronomy, Warsaw), 21
- Schneider, D. P., Young, P. 1980, *ApJ*, 238, 946
- Schild, H., Dumm, T., Mürset, U., et al. 2001, *A&A*, 366, 972 (S01)
- Shafter, A. W. 1983, *ApJ*, 267, 222
- Skopal, A., Djurašević, G., Jones, A., Rovithis-Livaniou, E., Rovithis, P. 2000a, *MNRAS*, 311, 225
- Skopal, A., Pribulla, T., Wolf, M., Shugarov, S.Y., Jones, A. 2000b, *Contrib. Astron. Obs. Skalnaté Pleso*, 30, 29
- Stone, R. P. S., Baldwin, J. A. 1983, *MNRAS*, 204, 347
- Thackeray, A.D., Hutchings, J.B. 1974, *MNRAS*, 167, 319 (TH74)
- Van Winckel, H., Duerbeck, H. W., Schwarz, H. E. 1993, *A&AS*, 102, 401
- Vassiliadis, E. & Wood P. R. 1993, *ApJ*, 413, 641
- Walder, R., Follini, D. 2000, in *Thermal and Ionization Aspects of Flows from Hot Stars: Observations and Theory*, ed. Henny J.G.L.M. Lamers, & A. Sagar, *ASP Conf. Ser.*, 204, 331